Sustainable and Healthy Communities through Integrating Mobility Simulations in the Urban Design Process

Center for Transportation, Environment, and Community Health
Final Report

by
Timur Dogan, Samitha Samaranayake
January 27, 2021

DISCLAIMER

The contents of this report reflect the views of the authors, who are responsible for the facts and the accuracy of the information presented herein. This document is disseminated in the interest of information exchange. The report is funded, partially or entirely, by a grant from the U.S. Department of Transportation's University Transportation Centers Program. However, the U.S. Government assumes no liability for the contents or use thereof.

TECHNICAL REPORT STANDARD TITLE PAGE

1. Report No.	2.Government Accession No.	3. Recipient's Catalog No.

4. Title and Subtitle	5. Report Date
Sustainable and Healthy Communities through Integrating Mobility Simulations in the Urban Design Process	January 27, 2021
	6. Performing Organization Code

7. Author(s)	8. Performing Organization Report No.
Timur Dogan (https://orcid.org/0000-0003-0749-8465) Samitha Samaranayake(https://orcid.org/0000-0002-5459-3898)	

9. Performing Organization Name and Address	10. Work Unit No.
Department of Architecture, Cornell University, 129 Sibley Dome, Cornell University, Ithaca, NY 14853	
	11. Contract or Grant No. 69A3551747119

12. Sponsoring Agency Name and Address	13. Type of Report and Period Covered
U.S. Department of Transportation 1200 New Jersey Avenue, SE Washington, DC 20590	Final Report 10/01/2019– 12/31/2020
	14. Sponsoring Agency Code US-DOT

15. Supplementary Notes

16. Abstract

Rapid urbanization and new global construction estimated to be 250x NYC by 2050 is increasing traffic congestion, pollution, and related health threats. Thus, it is imperative that we develop new modeling capabilities that allow urban designers to quantify the performance of mobility solutions, sustainability, public health impacts, pedestrian thermal comfort and pollution exposure during the earliest stages of a design process. Embedded in a generative, performance-driven design process, such a tool can significantly facilitate the design of healthy and sustainable urban habitats that promote active mobility.

Outdoor thermal comfort simulation simulations rely on the mean radiant temperature (MRT) seen by pedestrians as an important input that remains difficult to compute. Especially for large urban models, computing relevant surface temperatures and radiation fluxes that make up the MRT is a daunting task in terms of simulation setup and the computational overhead. We propose a new algorithm to estimate exterior surface temperatures of building facades, roofs, and ground surfaces in an arbitrary urban 3D model.

17. Key Words	18. Distribution Statement
Walkability, active mobility, urban design, computational design, modeling, software	Public Access: Conference Proceedings and Journal Paper. Free software downloadable from urbano.io

19. Security Classif (of this report)	20. Security Classif. (of this page)	21. No of Pages	22. Price
Unclassified	Unclassified		

Form DOT F 1700.7 (8-69)

Abstract

Outdoor thermal comfort simulation simulations rely on the mean radiant temperature (MRT) seen by pedestrians as an important input that remains difficult to compute. Especially for large urban models, computing relevant surface temperatures and radiation fluxes that make up the MRT is a daunting task in terms of simulation setup and the computational overhead. We propose a new algorithm to estimate exterior surface temperatures of building facades, roofs, and ground surfaces in an arbitrary urban 3D model. The algorithm discretizes all model surfaces and clusters them by material properties and sky and sun exposure to reduce computational complexity. The model setup is fully automated, and the algorithm is implemented in the popular Rhino3d CAD environment. We demonstrate the accuracy of the algorithm by comparing both the resulting external surface temperatures against a high-fidelity simulation and the final MRT against real-world measurements. We report an RMSE of 1.8°C and 2.0° C, respectively, while reducing simulation times by a factor of ~80. Envisioned applications of the algorithm range from rapid microclimate simulations in fast-paced urban design processes to large scale urban comfort evaluation of existing cities.

Keywords

Comfort, Surface-Temperature, Mean-Radiant-Temperature, Urban, Design, Microclimate

Introduction

Cities will be under particular climatic stress due to global warming compared to rural areas. (Krayenhoff et al., 2018) have shown that urban expansion has a significant effect on urban heat islands under the nonlinear relationship of all parameters relevant to the urban energy balance. Rising temperatures in cities will not only increase the energy demand of buildings for space cooling (Liu et al., 2019), in many climate zones, it also will worsen the outdoor thermal comfort of outdoor spaces (Allegrini et al., 2013) and put additional stress on public health in climates that already experience hot summers (Metzger et al., 2010).

Two processes with respect to the radiative heat exchange are particularly important for the built environments' contribution to the urban energy balance. First, street canyons and the reflections from buildings trap heat from incoming short-wave radiation. At the same time, the sheltering effect among the buildings decreases not only the view corridors but also decreases the long-wave radiation exchange with the sky. Ultimately, both processes lead to an increase in the ambient temperature (Luo et al., 2020) in high-density urban areas. Besides the urban form and density, materiality (Coutts et al., 2010), as well as the amount of green and blue infrastructure (Grilo et al., 2020), can significantly alter the urban microclimate. For example, high-albedo pavements are able to reduce the air temperature by 1.9°C, while surface temperatures decreased by 12°C (Santamouris et al., 2012). In another study, (Gagliano et al., 2017) found that green areas, such as green roofs, can be used as urban heat island (UHI) mitigation strategies by significantly decreasing external surface temperatures of up to 16°C. This shows that urban designers and planners have many degrees of freedom to mitigate the negative effects of rising urban temperatures using passive methods and informed design interventions such as high-albedo roofs and surfaces (Konopacki et al., 1998), vegetation, and evaporative cooling (Grilo et al., 2020). To plan and optimize such interventions, fast and easy-to-use tools that allow modelers to assess design proposals are necessary.

Literature review

While the theory behind urban microclimate modeling is well established, the research community usually approaches those problems from different scales ranging from mesoscale to microscale. The first controlled urban surface-atmospheric model comparison was carried out by (Grimmond et al., 2010). For example, mesoscale models use a combination of Weather Research and Forecasting Model (WRF) and Large Eddy Simulation (LES) as a method for atmospheric simulations that range from a 10 km cell size to ~50 m cell size (Talbot et al., 2012). However, mesoscale models are not able (and are not intended) to resolve detailed building geometries due to their limitation in cell size. This also precludes them from being able to assess the pedestrian space around the buildings.

When working with smaller length scales such as a pedestrian environment, models that work on the microscale are better suited. In this category, several models have been introduced in the literature whose fidelity increased over the years due to the increase in computational resources. In 2007, (Matzarakis et al., 2007) introduce a tool called RayMan that was later validated by (Lee

& Mayer, 2016), which achieved an RMSE of 12.6°C against measurements in a temperate climate. They reported that the missing long-wave radiation exchange emitted by surrounding surfaces and the low number of short-wave reflections leads to large errors at low sun angles as they are especially important at such angles. At the same time, (Krayenhoff & Voogt, 2007) introduce a three-dimensional (3-D) urban energy balance model, Temperatures of Urban Facets in 3-D (TUF-3D), that incorporates both short-wave and long-wave radiative fluxes and report a wall-averaged surface temperature RMSE of 4.0°C. Asawa et al. (2008) followed by implementing a design tool capable of long-wave radiation exchange. However, no comparison against measurement data was carried out. In 2010, the Solar Long-wave Environmental Irradiance Geometry model (SOLWEIG) was introduced (Lindberg et al., 2008) that takes into account short- and long-wave radiant fluxes for which an RMSE of 4.8°C for the T_{mrt} is reported. Yang & Li (2013) developed a voxel-based Model for Urban Surface Temperature (MUST). Their results show an RMSE of about 26 W/m^2 during the daytime, while an RMSE of 20 W/m^2 is achieved during nighttime. For surface temperatures, no RMSEs are reported, but comparisons of measured and observed data show differences of up to 5°C in the worst case for an east facade. In 2017, (2017) coupled *ENVI-met* with the *TRNSYS* environment to estimate the T_{mrt} for an idealized street canyon. Unfortunately, no rigorous error statistic has been provided, and the workflow is not feasible for large urban models where potentially hundreds of different canyon configurations would need to be set up manually in separate TRNSYS models. In 2018, (Nice et al., 2018) developed VTUF-3D, an extension of the previously TUF-3D model, taking into account radiative fluxes from vegetation.

In parallel to those developments, comparisons of those software packages have been made. A model comparison against measured data was carried out by Gál & Nice (2020), which compares the *VTUF-3D* approach, *ENVI-met*, and an approach carried out with *Radiance* and *EnergyPlus.* They found that *ENVI-met* systematically underestimated the T_{mrt} at nighttime and when surfaces are shaded.

Efforts have also been made to integrate the long-wave radiation exchange models into existing building energy simulation packages. Here, Evins et al. (2014) and Miller et al. (2015) attempted to enhance EnergyPlus' capabilities by coupling it with the existing microclimate software packages *ENVI-met* and *CitySim*. Both studies found that the incorporation of long-wave radiation exchange has a significant impact on heating and cooling loads, while at the same time reporting

a difference in external surface temperatures of 6 and 10°C, respectively. In 2020, Luo et al. (2020) drew from those findings and implemented a more detailed long-wave radiation exchange model directly into EnergyPlus. By default, EnergyPlus accounts for the long-wave radiative exchange to the sky, the ground, and surrounding air, see Figure 1; hence, leaving the long-wave heat exchange between the building and other buildings in the vicinity unaccounted for, contrary to reports by (Mackey et al., 2017).

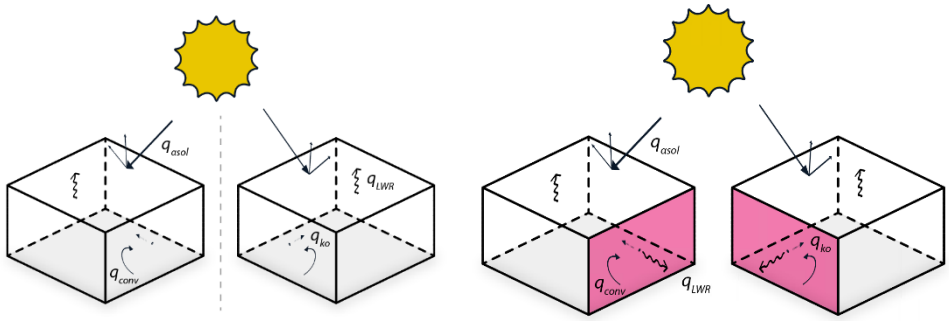

Figure 1: Scheme of outside surface heat balance with (right) and without (left) long-wave radiative fluxes between buildings.

We can write this energy balance (DoE, 2010):

$$q''_{\alpha sol} + q''_{LWR} + q''_{conv} - q''_{ko} = 0 \qquad (1)$$

Here, $q''_{\alpha sol}$ is the absorbed direct and diffuse solar (short wavelength) radiation heat flux, q''_{LWR} is the exterior surface long-wave radiation flux, q''_{conv} is the convective flux exchange with outside air, q''_{ko} is the conduction heat flux into the wall.

$$q''_{LWR} = \varepsilon\sigma F_{gnd}\left(T^4_{gnd} - T^4_{surf}\right) + \varepsilon\sigma F_{sky}\left(T^4_{sky} - T^4_{surf}\right) + \varepsilon\sigma F_{air}\left(T^4_{air} - T^4_{surf}\right) \qquad (2)$$

Here, ε is the long-wave emittance of the surface, σ is Stefan-Boltzmann constant, F_i are view factors between the surfaces, and T_j are the corresponding temperatures.

In the EnergyPlus 8.8 release, work by Luo et al. (Luo et al., 2020) enabled the estimation of the long-wave heat exchange if appropriate view factors from every surface to every other surface (many-to-many relationship) if provided by the user. Extending this equation to an arbitrary number of surfaces that are in long-wave radiation exchange, we can write:

$$q''_{LWR} = \varepsilon\sigma\Big[F_{gnd}\left(T^4_{gnd} - T^4_{surf}\right) + F_{sky}\left(T^4_{sky} - T^4_{surf}\right) + F_{s_1}\left(T^4_{s_1} - T^4_{surf}\right) + \cdots + F_{s_n}\left(T^4_{s_n} - T^4_{surf}\right) + F_{air}\left(T^4_{air} - T^4_{surf}\right)\Big] \qquad (3)$$

To reduce modeling complexity and overhead to enter the many to many view factor relationships, modelers often consider building facades as a single large surface. Arguably, this may not be a

reasonable assumption as the surface temperatures may differ significantly due to varying exposure to solar radiation and air temperature (in the case of skyscrapers). For a downtown urban area, this difference in surface temperatures has been shown by (Ghandehari et al., 2018). Hence, a meaningful discretization of facades is crucial when striving for locally accurate results. As reported by (Yang & Li, 2013), reasonably subdividing all radiating surfaces, the many-to-many relationship between the surfaces leads to an $O(N^2)$ complexity in the worst case, rendering this modeling approach impractical, especially for large scale urban analysis.

Hypothesis

These observations motivated the authors to explore automated procedures to substantially simplify 3D exterior surface temperature simulations while maintaining high spatial and temporal fidelity of the results to capture local effects related to materiality, complex urban shading situations, and predominant long-wave radiative exchanges while accurately accounting for sheltering and radiation trapping effects observed in urban environments.

The research in this paper is based on the hypothesis that many surface sub-sets in an urban simulation model are exposed to comparable environmental boundary conditions and are made of similar materials. Further, we assume that solar exposure and material properties explain the largest variance of resulting surface temperatures, surfaces with sufficient similarity in materiality, and sun exposure can be clustered and represented with a single representative surface to compute the temperature vector. With this approach, urban simulation models with many thousands of small surface patches can be reduced to just a few hundred typical surfaces in the simulation without sacrificing accuracy as well as spatial and temporal fidelity of the results.

Methodology

Based on the hypothesis that calculating exterior surface temperatures can be accelerated and simplified without losing temporal and spatial fidelity needed in urban design processes is possible, we introduce a novel algorithm called the “Surfer” that uses a global sensitivity analysis and K-Means clustering to automatically reduce surface count and related complexity of an arbitrary urban surface temperature simulation model. An overview of the key algorithmic steps, their inputs and outputs are shown in Figure 2. The algorithm is then validated against simulated surface temperature time series (Step1), point in time thermography measurements on-site (Step2),

and finally, the predicted mean radiant temperatures are compared with an on-site measured time series of a globe thermometer.

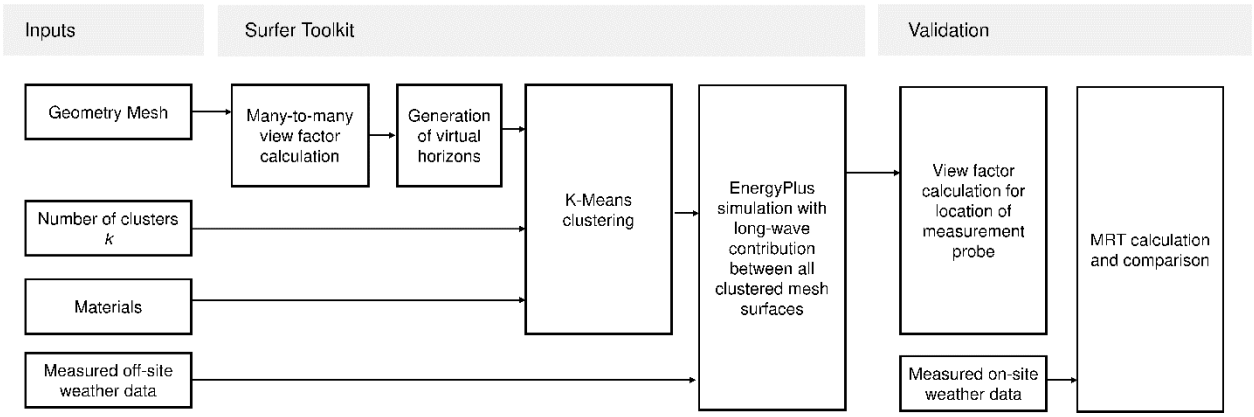

Figure 2: Flow chart of the proposed methodology

Global sensitivity analysis

To identify the dominant input parameters in the simulation of exterior surface temperatures in a given climate, we conduct an initial global variance-based sensitivity analysis (Saltelli et al., 2010; Sobol, 2001) for a set of five surfaces pointing upwards and in all main cardinal directions. We sample a parametrically defined two-layer construction with one exterior façade material and one inner layer of insulation material that is facing a constant interior temperature at 20°C. The construction features outlined in Table 1 are samples according to the Saltelli method using the SALib implementation (Herman & Usher, 2017) and are then simulated in EnergyPlus (Crawley et al., 2000). To aggregate the hourly temperature time series to a single number sensitivity metric, we use the average RMSE between the ambient and the external surface temperature. We generated 200 samples with the Saltelli scheme, which resulted in $N \cdot (2 \cdot D + 2) = 3200$ variants to simulated, where D is the number of features tested.

We present qualitative results of the analysis in Figure 3 as the resulting ranking of the input parameters as they are used to inform the clustering parameters that determine how model surfaces are grouped in the next step of the algorithm. We show parameter sensitivity averages for all surface orientations in Figure 3 (left). It shows that surface solar absorptance is by far the most significant parameter, explaining 79 % of the variance in the output, suggesting that surface orientation and shading patterns by urban context have a significant effect. Figure 3 (right) shows feature sensitivity for North facing surfaces that see a significantly smaller amount of solar radiation. Here, other construction properties such as conductivity, density, specific heat, and

thickness become important, suggesting that north-facing and heavily shaded surfaces in the urban environment are susceptible to these features. An exhaustive set of second-order sensitivity results is given in **Error! Reference source not found.** in the appendix.

Features	Bounds
Conductivity	[0.0001, 4.9]
Density	[10, 5000]
SpecificHeat	[101, 5000]
ThermalAbsorptance	[0.05, 0.95]
Solar Absorptance	[0.05, 0.95]
Thickness	[0.02, 0.3]
InsulationThickness	[0.01, 0.2]

Table 1: Feature bounds of the global SA

Feature	S1	S1_conf	ST	ST_conf
Conductivity	0.011	0.046	0.077	0.062
Density	0.002	0.037	0.059	0.021
SpecificHeat	0.004	0.045	0.084	0.076
ThermalAbsorptance	0.073	0.066	0.105	0.025
SolarAndVisibleAbsorptance	0.624	0.166	0.794	0.166
Thickness	-0.003	0.025	0.018	0.008
InsulationThickness	0.004	0.009	0.003	0.001

Table 2: First and total order sensitivity indices– façade averages

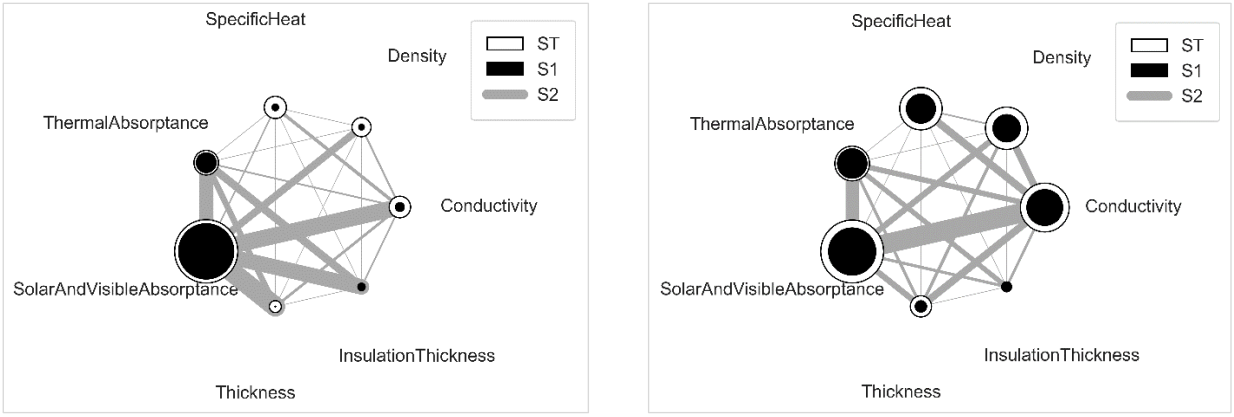

Figure 3: Qualitative radial plot of parameter sensitivity and interaction averaged across all surfaces (left) and north-facing (right) for external surface and dry bulb temperatures.

Model input

Geometry

Algorithm inputs are surfaces or poly-surfaces representing the building facades, roofs, as well as pavement, and other ground surfaces. Each surface is paired with construction properties and a window to wall ratio. These surfaces are then discretized into smaller surface-patches based on a user-defined edge length. The default is set to 3 m that mostly yields quads of approximately 3x3 dimensions. This setting is assumed throughout the paper. To test and validate the proposed algorithm, we model a parking lot framed by a series of larger buildings located at the authors' home institution (Figure 4). The aerial view in Figure 4 also marks the location of the microclimate logger that we use for the comparison of measured and simulated MRT in the validation section. The model consists of 70 surfaces that describe the roofs, facades, and ground surfaces. Discretized into 3x3 quads, this yields approximately 3000 surface patches (Figure 5).

Weather data

The climate data used in the sensitivity analysis and Step1 of the validation is a TMY3 dataset for Syracuse, USA (Warm-summer humid continental climate (Dfb), according to the Köppen classification (Kottek et al., 2006)). For the validation Step2 and Step3 that compare on-site measurements against simulation outputs, we use data measured by an on-site HOBO weather station that monitors the microclimate at the marked location in Figure 4. Off-site weather data, used as model input, was collected at a nearby, unobstructed weather station operated by the Northeast Regional Climate Center, 3 km from the author's home institution (GFR Weather Station, NRCC Cornell). Both on-site and off-site stations record several variables, including pressure, dry bulb temperature, relative humidity, global horizontal solar radiation, wind velocity, wind direction, and the dew point temperature, see Table 3. The direct/diffuse radiation split was calculated according to the methodology by (Reindl et al., 1990).

MRT measurement

The on-site station was outfitted with an additional temperature sensor covered with a ping-pong ball to measure MRT. While we followed existing best practice guidelines for MRT measurements by (De Dear, 1988), who reports that ping pong balls are a suitable means of measuring the mean radiant temperature if the wind velocity is below 1.2 m/s, there may exist convective heat losses influencing the measurement. Measuring the MRT with globe thermometers introduces a tradeoff between the time the thermometer reaches the radiative equilibrium (the response time) and the error due to convective heat transfer losses (accuracy). A small globe would reach the equilibrium faster through an increased convective heat transfer coefficient, thereby increasing the effect of separation of air temperature form the globe temperature and increasing the influence by variations in air velocity. This renders the globe thermometer less capable to resolve radiation inputs accurately. (Thorsson et al., 2007). However, Nikolopoulou et al. (n.d.) suggest the ping pong balls are a good choice for globe thermometers with a response time smaller than 5 min due to their robustness and their matte surface characteristics. Besides that, Thorsson et al. (2007) suggest a measurement aggregation to a 5 min mean value (10 minutes show diminishing returns) to avoid scattering of values due to rapid changes in radiation fluxes which was followed in our approach. DeDear (1988) reported accuracies ranging from -1.2 K to +0.8 K for ping pong globe thermometers depending on the environmental conditions.

Table 3: Measured environmental variables and their resolution and accuracy.

Variable	Unit	Instrument	Resolution	Accuracy
Dry Bulb Temperature	°C	HOBO S-TMB-M0xx	<0.03°C from 0° to 50°C	< ±0.2°C from 0° to 50°C
Relative Humidity	-	HOBO S-THB-M002	0.1% RH	+/- 2.5% from 10% to 90% RH , to a maximum of +/- 3.5% including hysteresis at 25°C; below 10% and above 90% ±5%
Wind velocity	m/s	HOBO S-WCG-M003	0.4 m/s	±0.8 m/s or ±4% of reading, whichever is greater
Wind direction	deg	HOBO S-WCG-M003	1 deg	0.2 to 3 m/s: ±4 degrees >3 m/s: ±2 degrees
Globe temperature	°C	HOBO S-TMB-M0xx; white ping pong ball	<0.03°C from 0° to 50°C	< ±0.2°C from 0° to 50°C
Global Solar Radiation	W/m^2	HOBO S-LIB-M003	1.25 W/m^2	±10 W/m2 or ±5%, whichever is greater in sunlight; Additional temperature-induced error ±0.38 W/m2 /°C from 25°C
Surface Temperature	°C	FLIR Imager E6390	80x60IR 45°x34° FOV resolution, <0.15°C/150mK from -20°C to 250°C	±2°C (±3.6°F) or ±2% of reading, for ambient temperature 10°C to 35°C (50°F to 95°F) and object temperature above 0°C (32°F)

Material properties

The constructions used for the study area are (1) a 5 cm asphalt (Conductance: 0.75 [W/m K], Density: 2350 [kg/m3], Specific Heat: 920 [J/kg K]) with a 20cm generic concrete underlay used for the roofs and pavement as well as (2) a 20cm yellow brick façade (Conductance: 0.56 [W/m K], Density: 1200 [kg/m3], Specific Heat: 1000 [J/kg K]) with interior insulation. Solar absorptance for both exterior material layers is estimated by using a CIBSE color chart to determine the visible reflectance of the materials. We assume a solar absorptance of 0.8 for the asphalt and 0.7 for the yellow brick façade. This is also in good agreement with other data tables that provide an order of magnitude ranges for solar absorptance of different materials (Engineering ToolBox, 2009). The glazing is assumed to be a generic double-pane clear glass with a U-Value of 2.76 [W/m2 K], SHGC of 0.76, and a T_{vis} of 0.81.

Figure 4: Aerial view of the case study area showing a parking lot framed by larger buildings located at the authors' home institution.

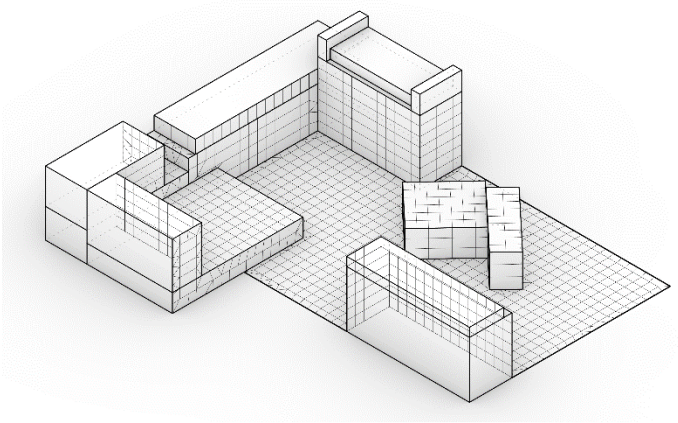

Figure 5: 3D representation of the simplified CAD model showing the discretization of building and ground surfaces into 3x3 m patches.

Clustering

The surface-patches that are generated by the model discretization step described above are then analyzed and clustered by their similarity using K-Means (MacQueen, 1967). Based on the findings from the initial sensitivity analysis, we implement clustering using exterior surface solar absorptance (direct sun), thermal absorptance (long-wave), conductivity, density, and specific heat as distinguishing parameters. Further, surface orientation as a three-dimensional vector and overshadowing patterns are included in the clustering procedure. The overshadowing patterns for each surface-patch are summarized by eight elevation angles forming a virtual horizon for each patch. These angles are computed using ray-model intersection tests in user-defined degree steps (five degrees is the default) for azimuth and elevation at each surface patch centroid. The intersection test results are then used to determine the average horizon height stored in an array of eight elevation angles. Figure 6 (left) illustrates a virtual horizon that is used as an input for the clustering, whereas Figure 7 shows the mesh surfaces colored by their cluster group ID.

It is well known that the K-Means algorithm fails for input data in spherical clusters. To prevent the occurrence of this weakness, we are forcing each construction material into a cluster, thereby essentially running the algorithm twice.

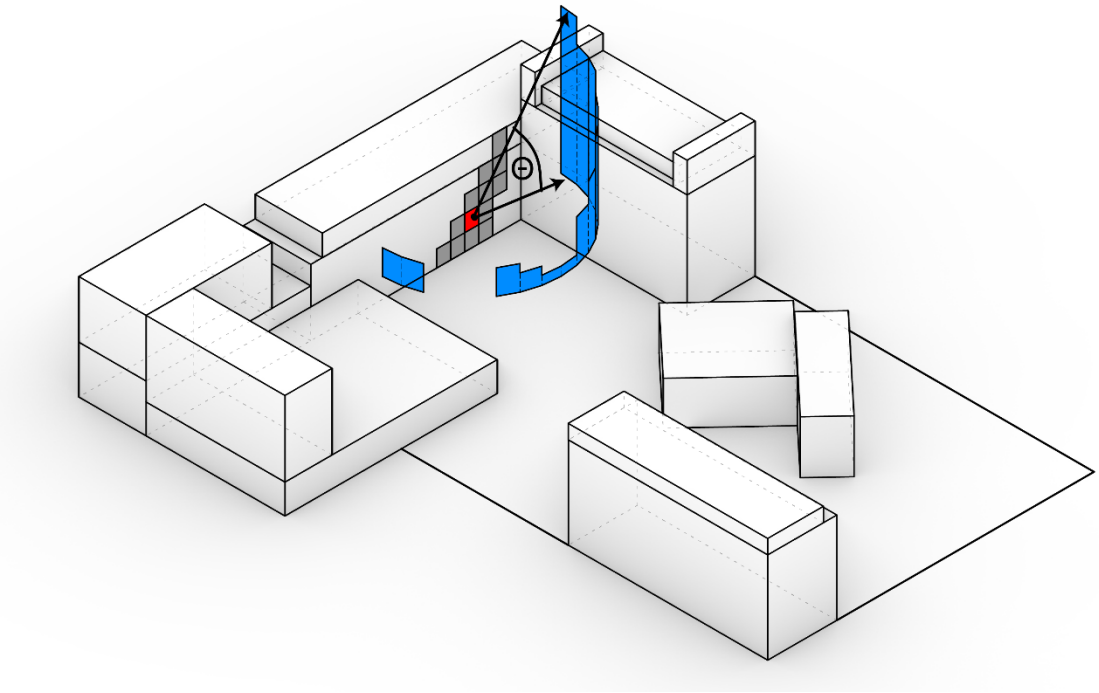

Figure 6: Virtual horizon for a shading geometry shoebox highlighted.

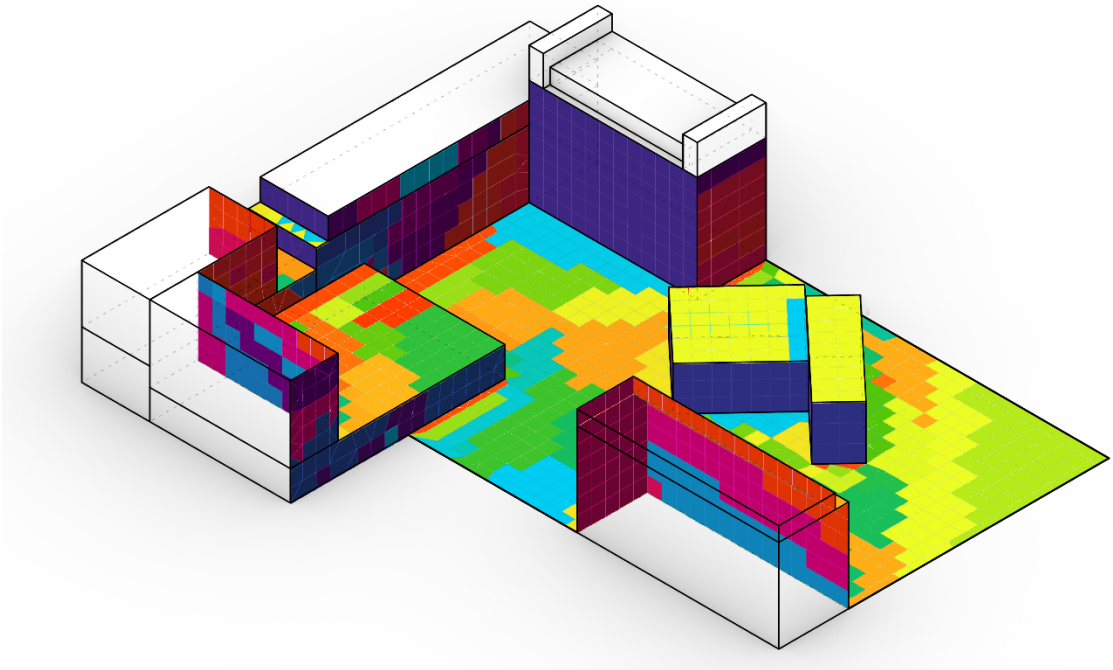

Figure 7: Surfaces binned into clusters with the K-Means algorithm with their enumerated cluster centroids (K = 80).

View Factors

View factors between the different surface patches are required to model the long-wave radiative exchange between all simulated surfaces. We compute these view factors according to Equation 4 provided below (Hardy & Steeb, 2008):

$$F_{ij} = V_{ij} \frac{A_j \cos \phi_i \cos \phi_j}{\pi r^2} \quad (4)$$

We cast rays from various points on patch j to patch i. The percentage of the rays that make it from patch j to patch i are recorded as V_{ij}. For small surfaces, a single ray is sufficient and serves as an occlusion test. We have $V_{ij} = V_{ji}$. Let r be the distance between the centers of the patches, and then we approximate the view factor by Equation (4). To further reduce computational overhead, the user can specify a cut-off value (>0.0001 is the default) to skip the occlusion test for surface pairs where the resulting view factor would be insignificant.

It is important to note that we compute the view factor relationships between all small surface patches. For large models, storing this information can lead to significant memory use (Yang & Li, 2013). We circumvent this problem since we can immediately aggregate the patch-to-patch view factors into cluster-to-cluster view relationships. This significantly reduces the amount of view factor pairs that need to be stored in memory.

Surface Temperature Simulation

Once clustering and view factor computation are complete, the surfer algorithm can export the representative surface patches (cluster centroid) and the aggregated view factor relationships between the cluster centroids. To compute the cluster-centroid surface temperature time series, we implement the surface temperature simulation using EnergyPlus; the clustering method itself is, however, simulation-tool-agnostic and could also utilize other simulation software packages like TRNSYS (Beckman et al., 1994) or simpler models like the CIBSE admittance method (Davies, 1994).

To prepare the model for EnergyPlus, we place a shoebox (Dogan & Reinhart, 2017) at the location of each cluster centroid, see Figure 8. The shoebox assumes the footprint of the surface patch (3x3m). A small window surface is added, and the opaque and glazing construction is assigned. An interior boundary condition of 20°C is assigned to the surfaces. To accurately model the shading effect of the urban context, all original model surfaces are added as shaders. Exterior surface long-wave radiative exchange is configured with the “surrounding surfaces” object and an

Energy Management System (EMS) script to synchronize simulated surface temperatures internally. In the current implementation of EnergyPlus, this is only possible with a one-time-step lag (Luo et al., 2020). Finally, the entire model is exported as a single IDF file (Input File) and simulated with EnergyPlus through the Rhino and Grasshopper plugin ClimateStudio (Solemma LLC, 2019). The results obtained are surface temperature time series for the opaque construction and the glazing surface for each cluster centroid.

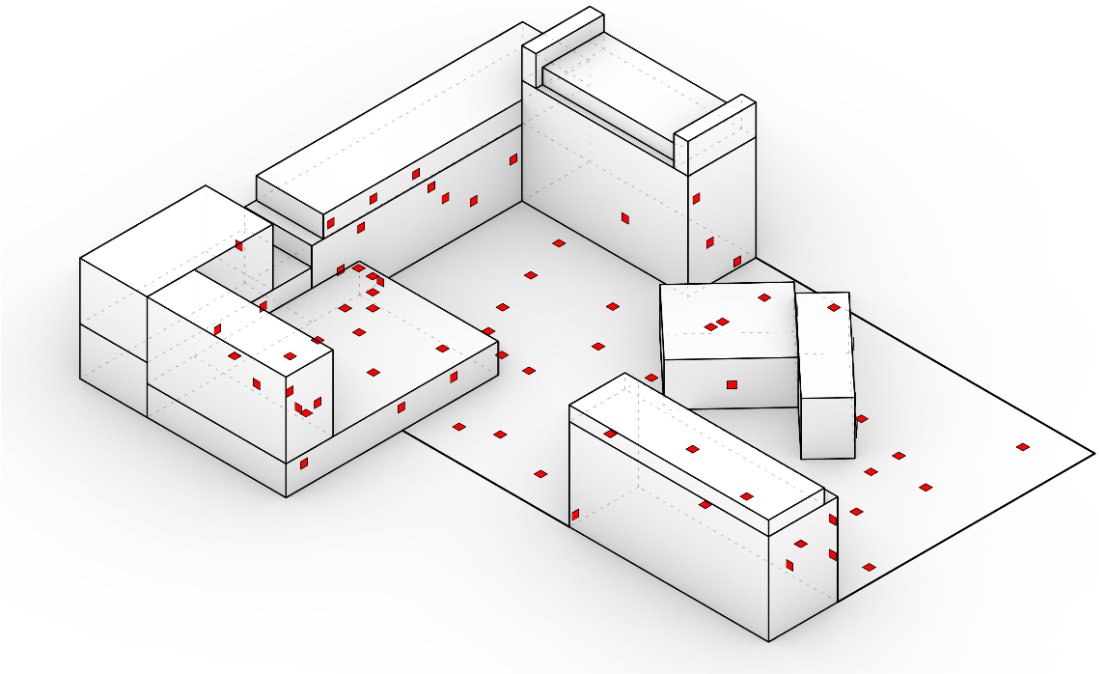

Figure 8: Sampled surfaces for which radiative exchange is simulated for K = 40.

Mean Radiant Temperature

The mean radiant temperature (MRT) is an important input for thermo-physiological comfort indexes such as physiological equivalent temperature PET (Mayer & Höppe, 1987) or universal thermal climate index UTCI (Blazejczyk et al., 2013). It is defined as the view factor (F) weighted mean temperature of all the surfaces surrounding a body. It is, therefore, a desirable result that can be calculated based on the surface temperatures predicted with the Surfer algorithm. The MRT can be predicted (Thorsson et al., 2007) using three major components: (1) the surface temperatures of all surrounding building and ground surfaces $T_{surf,j}$, (2) the sky temperature T_{sky}, and (3) the solar radiation gain that acts on a person in direct sunlight. These three components are combined to compute the MRT for every hour *h* and every probing location *i* according to Equation (5):

$$MRT_{h,i} = T_{sky,h} \cdot F_{sky,i} + \sum_{j=0}^{n} (T_{surf,h,j} \cdot F_{surf,i-j}) + \Delta MRT_{h,i} \quad (5)$$

(1) Surrounding surface temperatures

The effect of the surface temperatures surrounding a person's location requires to compute a set of view factors from the probing point (person's location or, in our case, the location of the microclimate logger as indicated Figure 4) to all surface-patches in the model using Equation 4. The resulting view factors are then aggregated within each cluster, and the surface temperature that is modeled for each cluster centroid is extracted.

(2) Sky temperature

Similarly, for each probing point, a sky view factor $F_{sky,i}$ can be approximated based on the sum of all surface view factors according to:

$$F_{sky,i} = 1 - \sum_{j=0}^{n} (F_{surf,i-j})$$

The sky temperature T_{sky} can be extracted as a simulation result from any of the surface temperature simulations conducted in EnergyPlus. If necessary, the sky temperature can also be calculated directly using sky emissivity and the horizontal infrared radiation intensity as defined in the EnergyPlus Engineering Reference (DoE, 2010).

(3) Solar gain MRT offset

The solar radiation gain can be described as a temperature offset ΔMRT_{ds} that is calculated using the Effective Radiant Field (ERF) (Arens et al., 2015), which we adapted for an outdoor setting and from which we derived ΔMRT_{ds}. For this, we assume a "standing" posture which refers to a value of 0.725 for f_{eff}, a total solar transmittance t_{sol} of 1, and the fraction exposed to the sun to be 0.5.

$$E_{diff} = f_{eff} \cdot f_{svv} \cdot 0.5 \cdot t_{sol} \cdot I_{diff} \qquad E_{direct} = f_p \cdot t_{sol} \cdot f_{bes} \cdot I_{dir}$$

$$E_{solar} = E_{diff} + E_{direct} \qquad ERF = E_{solar} \cdot \frac{sw_{abs}}{lw_{abs}} \quad (6)$$

$$\Delta MRT = \frac{ERF}{hr \cdot f_{eff}}$$

To compute the irradiance that is used as an input for the ERF, we implemented a Radiance-based Two-Phase (DDS) method (Subramaniam, 2017). The DDS approach was chosen because it provides a better spatial resolution of the direct component. The Two-Phase DDS method is a daylight-coefficient-based simulation with an all-weather dynamic sky model (Perez Sky model). Instead of approximating the position and shape of the sun with few sky patches, we used 577 sun patches for the direct and diffuse simulation and 2305 direct sun patches. The Radiance simulations use three ambient bounces and 5000 ambient divisions. The illuminance is a linear combination of (1) an annual daylight coefficient simulation, (2) annual direct-only daylight coefficients, and (3) an annual sun-coefficients simulation (Bourgeois et al., 2008):

$$E = C_{dc} \cdot S - C_{dcd} \cdot S_d + C_{sun} \cdot S_{sun}$$

where C_{dc} and S denote the daylight coefficient matrix and the sky vector, C_{dcd} and S_d denote the direct-sky coefficient and the direct sky matrix, and C_{sun} and S_{sun} denote the direct-sun coefficient and the sun matrix, respectively (Subramaniam, 2017).

Validation

To validate the proposed simulation approach, we compare the simulated results in three steps:
(1) We assess the influence of K (number of clusters) on the average surface temperature time series RMSE between all surfaces in a cluster, compared to its cluster centroid. We do this to introduce a measure for how much the cluster centroids differ from the simulated ground truth.
(2) We compare a predicted surface temperature against on-site observations using a thermal camera. (3) In a third step, we compare a predicted MRT time series against microclimatic measurements by an Onset HOBO sensor at the case study site; see Figure 4 for the measurement location. The 12-bit temperature sensor used is specified with an accuracy of < ±0.2°C from 0° to 50°C and a resolution of <0.03°C from 0° to 50°C.

Step 1: Surface temperature: Cluster result vs. simulation of all surfaces via Energy Plus

We simulate all surface patches individually and obtain surface temperature time series using EnergyPlus. In this simulation, we neglect the patch-to-patch long-wave radiation exchange. This dataset serves as ground truth to determine the cluster accuracy and computational overhead of our new method. We then use the proposed Surfer method to estimate surface temperature time series with different K-values ranging from 2 – 100 with increments of 2. We use the Elbow method as

a heuristic to choose a K-value, after which diminishing returns are not worth the additional computational cost (Thorndike, 1953).

Step 2: Surface temperature: Cluster result vs. thermography images

For K = 40, we calculate the surface temperatures of the facades and ground surfaces and compare them against thermography images taken on-site for one point in time and multiple view directions. The thermography images were taken with a FLIR E4 MSX Imager. The imager was calibrated using the onboard library of materials for the correct emissivity of the measured material. Dimensions were taken to determine the distance from the imager to the measured area and inputted into the imager as well. Thermal imagery results were compared with readings from an infrared thermometer to determine if they matched. Simulation results are reported with and without patch-to-patch longwave radiation exchange to verify the importance of this phenomenon.

Step 3: Mean radiant temperature: Cluster result vs. real-world measurement

For K = 40, we calculate hourly mean radiant temperature time series and compare them against real-world, on-site measurements of globe temperatures. The weather data input for the Surfer algorithm is a custom EPW file that was created from data collected at the off-site station. We use a window-to-wall ratio of 20 % to derive the mean radiant temperature from the surrounding surfaces at the measurement location, see Figure 4. To calculate the MRT considering convection effects, we use the equation (7 suggested by (Thorsson et al., 2007).

$$T_{MRT} = \left[\left(T_g + 273.15\right)^4 + \frac{1.1 \cdot 10^8 \cdot V_a^{0.6}}{\varepsilon \cdot D^{0.4}} \cdot \left(T_g - T_a\right) \right]^{0.25} - 273.15 \qquad (7)$$

Results

Step 1: Surface temperature: Cluster result vs. simulation of all surfaces via EnergyPlus

Figure 9 shows the RMSE errors between the cluster centroids and all surfaces in their respective cluster for window and façade temperatures over the number of clusters without patch-to-patch long-wave interactions. The figure illustrates that the façade RMSEs decrease non-linearly. They decrease quickly for $0 < K < 8$, less quickly for $8 < K < 40$, and we have diminishing returns for $K > 40$. The algorithm predicts surface temperatures with reasonable errors for $K > 40$, which led the authors to determine $K = 40$ as a reasonable number of clusters for this study. Figure 9 illustrates a worst-case error-band of an RMSE of 2°C for $K \geq 40$ for both facades and windows.

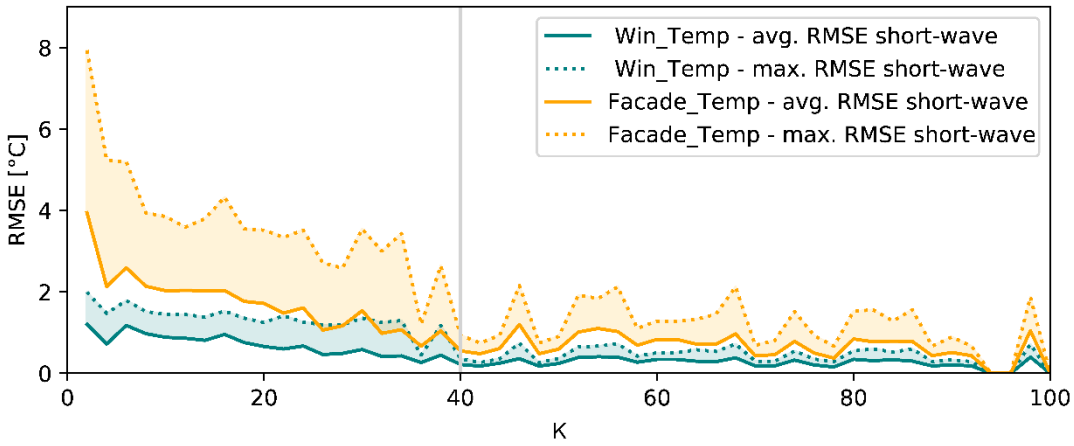

Figure 9: RMSE errors between cluster centroids and their cluster members for window and façade temperatures over the number of clusters without patch-to-patch long-wave interactions.

Figure 10 shows the average simulation time for short wave radiation-only and patch-to-patch long-wave simulation variants. Extrapolating the observed simulation times from Figure 10 for 1574 clusters (most accurate simulation possible) yields a hypothetical simulation around 85 min for short-wave & long-wave and simulation time of 50 min for short-wave-only.

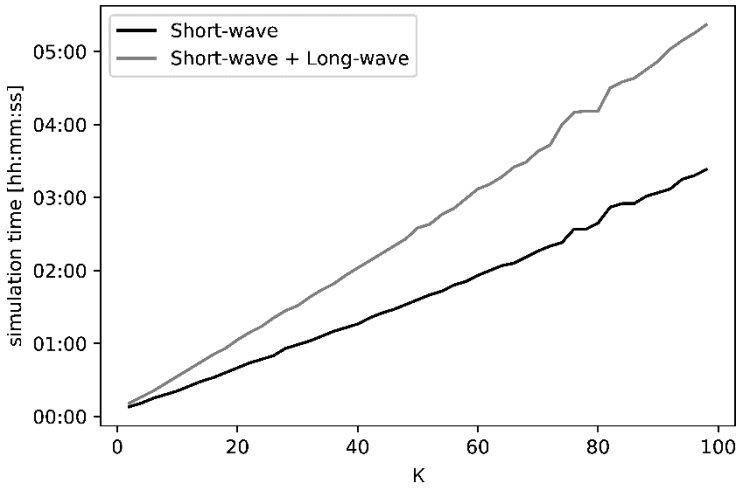

Figure 10: Simulation time with respect to the number of clusters for the K-Means algorithm.

Figure 11 shows the monthly diurnal average of external façade temperatures comparing the short-wave-only and the patch-to-patch long-wave radiation exchange approach implemented by our method. As expected, external surface temperatures differ most significantly from the dry bulb temperature during the summer months. For the external façade temperatures, the new approach shows differences in external temperatures of about 6°C in the summer months, whereas the difference during the winter months is around 3°C.

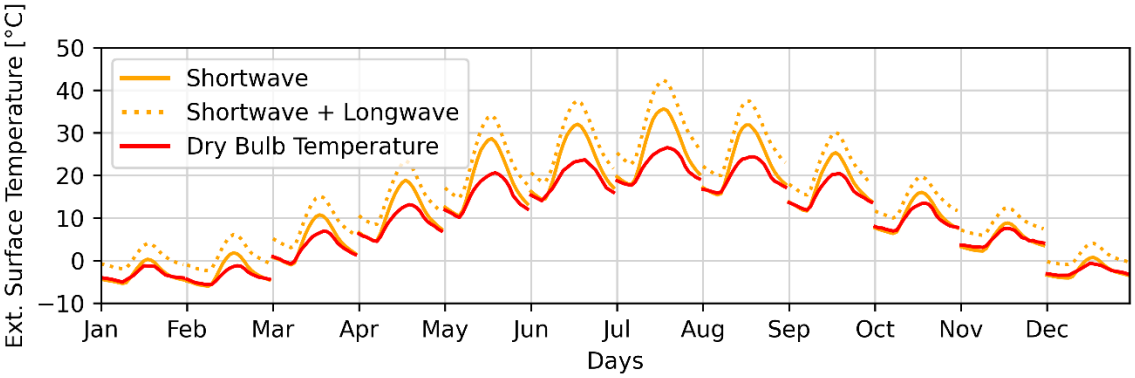

Figure 11: Monthly diurnal temperature averages of external façade temperatures.

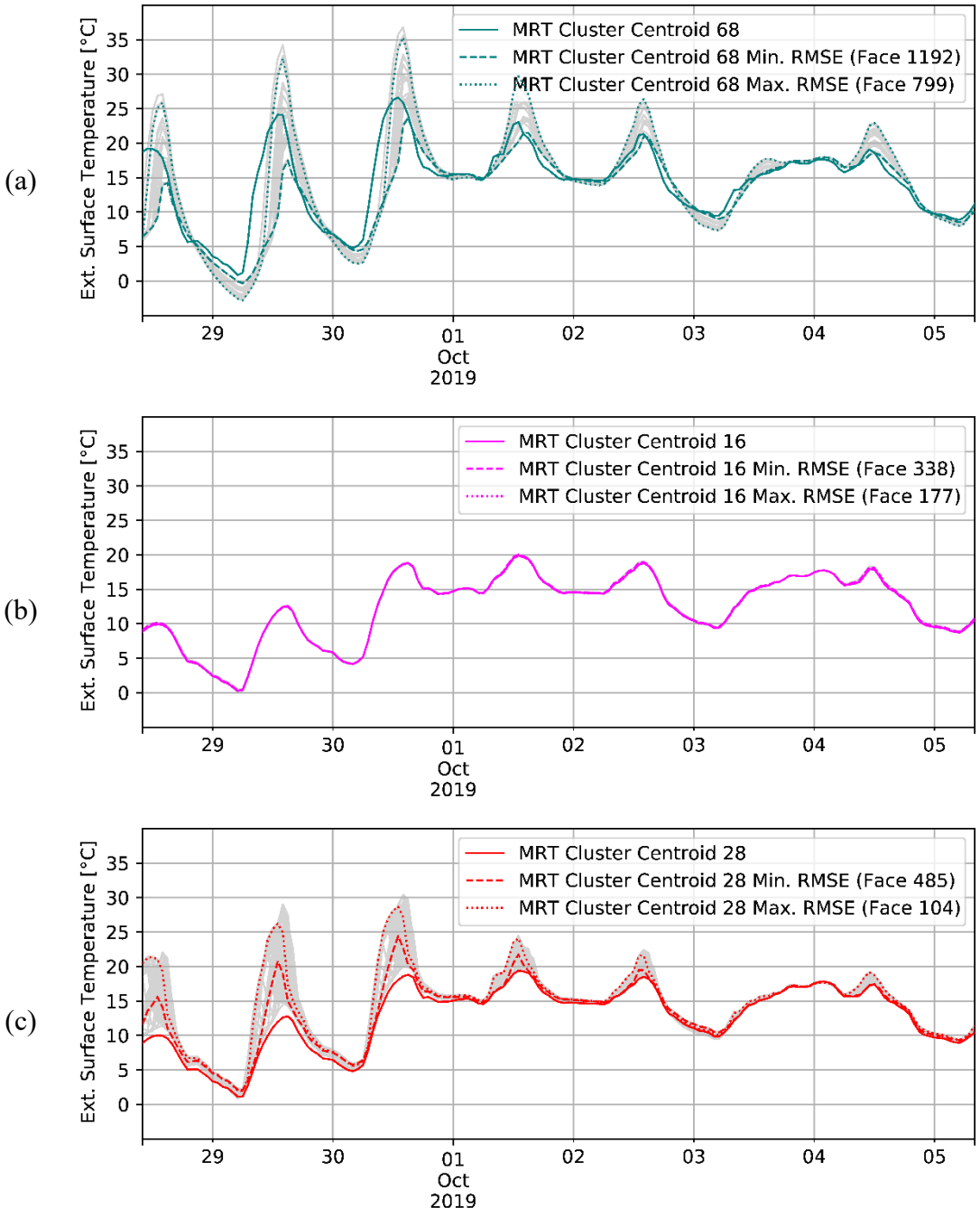

Figure 12: (a) Timeseries of three selected clusters oriented horizontally (teal), (b) vertical-north, showing negligible errors due to homogeneous cluster (magenta), and vertical-south (red). The dashed and dotted lines denote the mesh faces with the smallest and largest annual hourly RMSE within that cluster. All grey lines represent the remaining mesh faces in the respective cluster.

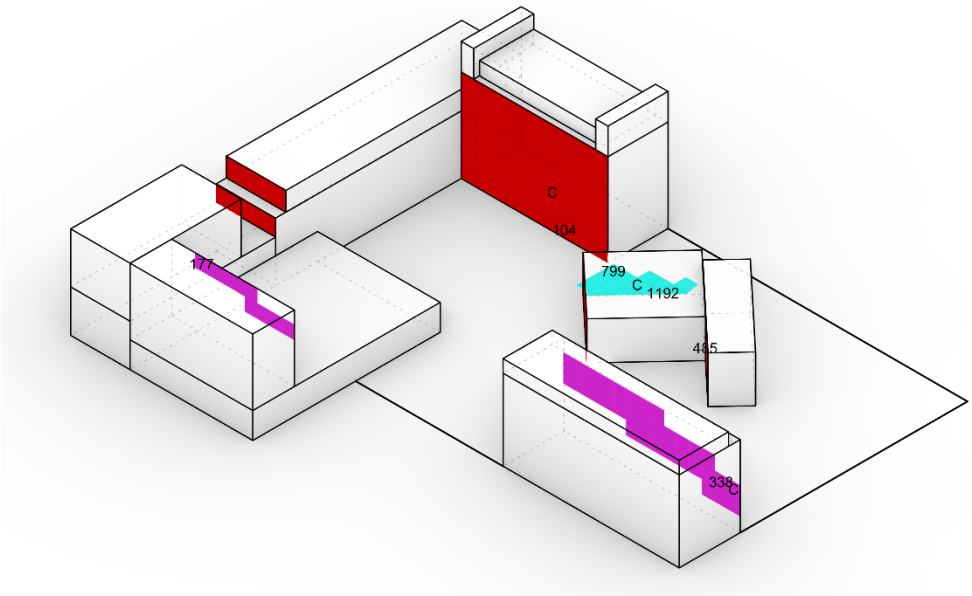

Figure 13: Selection of three clusters: horizontal (mesh face 68 - teal), vertical-north (mesh face 16 - magenta), and vertical-south (mesh face 28 - red) oriented. "C" denotes the centroid for each cluster. The denoted mesh faces illustrate the mesh faces with the smallest/largest annual hourly RMSE with respect to the respective cluster centroid.

In Figure 13, we illustrate three clusters with their cluster centroid and all mesh patches the cluster represents. We further show the patches with the smallest and largest annual hourly RMSE for their respective cluster centroid. The teal cluster is oriented horizontally, whereas the magenta and red cluster are vertical surfaces pointing North and South, respectively. Cross-referencing their location with their hourly time series in Figure 12, we see that the largest deviations (over and underprediction) exist for the cluster centroid for horizontal surfaces depending on whether they are directly exposed to the sun (Figure 12 (a)). Figure 12 (b) reveals that in-cluster RMSEs are negligible to the degree that all data points are perfectly overlapping for north-facing mesh faces. Figure 12 (c) shows smaller RMSEs compared to the horizontally oriented mesh faces; however, both the mesh face with the minimum and maximum RMSE overpredict the surface temperature.

Step 2: Surface temperature: Cluster result vs. thermography images

Figure 14 shows on-site thermography images in three directions around the on-site station. Table 4 contrasts the measured data with simulation results with and without long-wave radiation. The measurements, generally, are in good agreement with the simulation results when the longwave

radiative exchange is considered. The results for West (a) Bx1, Bx2, and Bx3 in Table 4 are particularly noteworthy. The regions West (a) Bx2 and Bx3 show the highly localized effect of long-wave radiation exchange.

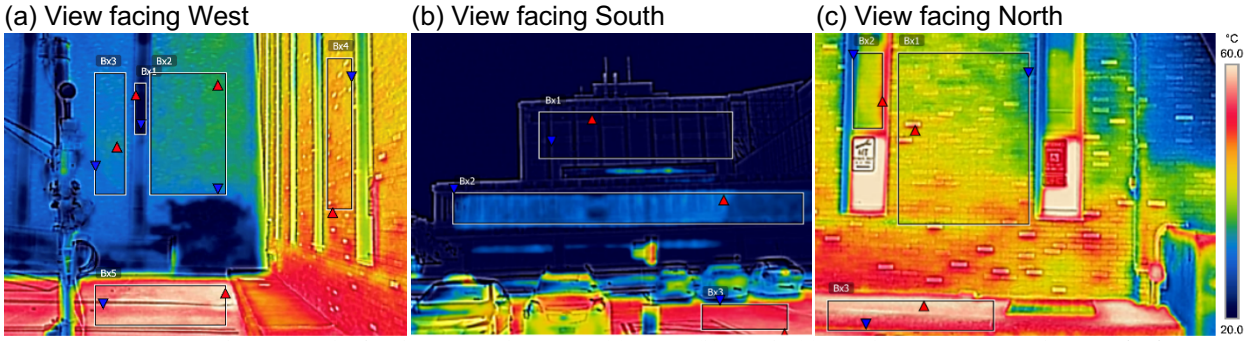

Figure 14: On-Site Thermography for three view directions (a) West, (b) South, (c) North. Images were taken on 9/19/2020 at 1:15 pm from the viewpoint of the microclimate station location marked in Figure 4.

Table 4: Surface temperatures measured using a FLIR thermal camera for 9/19/2020 at 1:15 pm. These readings are compared to the two simulation approaches with and without longwave radiation exchange.

Location	**Meas. Av.**	**Meas. Range**	**Sim.** (no longwave)	**Sim.** (with longwave)
West (a) Bx1 Window	21.0 °C	17.8 - 26.1 °C	21.0	21.0
West (a) Bx2 Brick	32.0 °C	28.2 - 33.3 °C	23.8	31.2
West (a) Bx3 Brick	30.8 °C	29.5 – 31.9 °C	23.4	29.4
West (a) Bx4 Brick	44.5 °C	41.0 -47.1 °C	37.1	43.2
West (a) Bx5 Ground	55.8 °C	52.1 – 60.7 °C	47.7	55.9
South (b) Bx1 Façade	11.7 °C	9.8 – 16.5 °C	20.7	23.9
South (b) Bx2 Façade	23.9 °C	19.0 - 26.6 °C	20.8	24.0
South (b) Bx3 Ground	46.3°C	21.0- 60.7 °C	47.5	57.1
North (c) Bx1 Brick	45.5 °C	41.3 – 50.0 °C	37.1	43.2
North (c) Bx2 Window	44.6 °C	35.9 – 50.1 °C	25.0	25.0
North (c) Bx3 Ground	55.8 °C	48.9 – 60.2 °C	47.7	55.9

Step 3: Mean radiant temperature: Cluster result vs. real-world measurement

Figure 15 compares the simulated MRT against the calculated MRT at the author's home institution for a week in October 2019. During this period, we observe an RMSE of 2.04°C for cloudless days and an RMSE of 2.23°C for days with sky cover > 0.1.

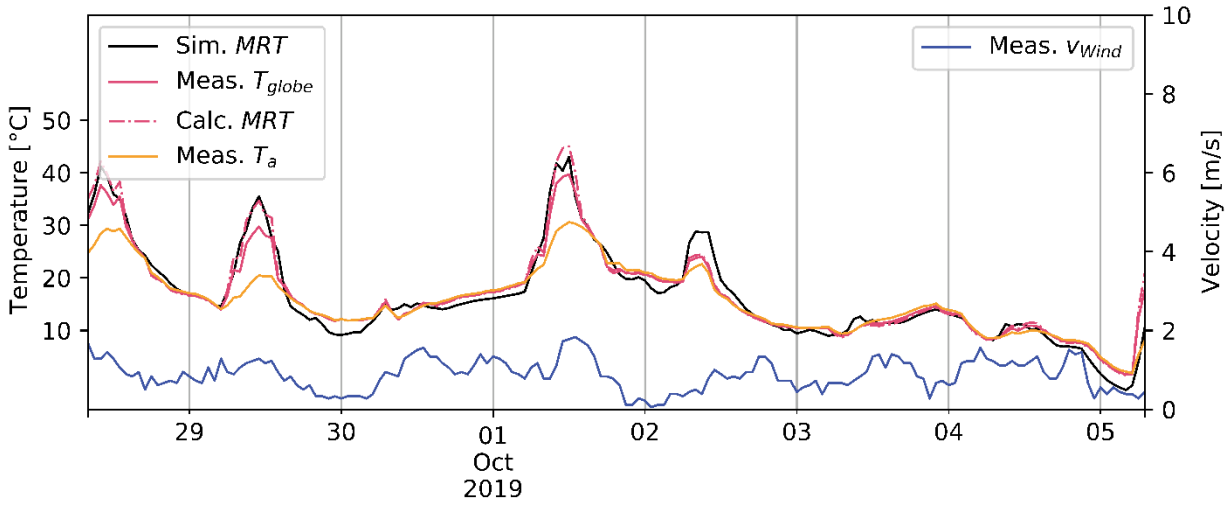

Figure 15: Measured Globe Temperature, calculated MRT (equation X), simulated MRT, and measured dry-bulb temperature (T_a) for a week in 2019.

Discussion

This research shows that it is possible to cluster external surfaces in an urban environment to speed up outdoor thermal comfort simulations while preserving a reasonable degree of accuracy and high spatial resolution. This effort allows for simulating long-wave radiation exchange between external building surfaces, which is especially important in summer months where simulation with and without longwave radiative exchange deviates most (see Figure 11). The computational expense of a many-to-many long-wave radiation exchange calculation would conventionally grow with $O(N^2)$ and thus is a computationally costly calculation for large scale urban models with many surface patches. Figure 9 shows that the K-Means algorithm with 40 clusters achieves an average RMSE of < 1°C for both external windows and façade temperatures, while Figure 10 shows a decrease in a simulation time of ~98% for the same number of clusters. In Figure 12, we sampled three clusters with different orientations and plotted the time series of the mesh series with the smallest and largest RMSE against their cluster centroids. The results confirm what the orientation and location of the clusters would suggest; that is, if the cluster is comprised of mesh faces that see a different amount of radiation during the day (teal cluster), the intra-cluster RMSEs are larger compared to a cluster that sees very similar exposure to radiation (magenta cluster).

This suggests that most RMSEs can be attributed to differences in when and how strong the solar radiation impulse is acting on a surface and, if desired, an even greater accuracy could be achieved by using a finer geometric resolution of the virtual horizon (Figure 6) as clustering input. We

would further like to acknowledge prevalent uncertainties in our model and its validation procedure that can help further explain the deviations observed in this study. While we followed existing best practice guidelines for mean radiant temperature measurements by (De Dear, 1988), who reports that ping pong balls are a suitable means of measuring the mean radiant temperature if the wind velocity is below 1.2 m/s, there may exist convective heat losses influencing the measurement. However, the measured wind velocity in Figure 15 does not suggest a significant error contribution.

When conducting the sensitivity analysis as a precursor to establish a feature set for the K-Means clustering algorithm, we only considered opaque surfaces. This decision was made because the window-to-wall ratio (WWR) for the building geometry in question was about 20 %. As the U-value for windows is generally much higher than it is for walls, the feature set for transparent surfaces will likely be different from the feature set for opaque surfaces. However, given the small WWR and the low RMSEs, we regarded the feature set as appropriate for this study. Moreover, a cluster number of K = 40 might not be ideal when simulating larger urban areas than the study assessed here. Further studies are warranted that assess both alternative clustering approaches (such as hierarchical clustering) for this purpose and to analyze whether the number of clusters generalizes for any size/complexity of input geometries.

This workflow stands in contrast to efforts made by the authors of tools such as ENVI-met or VTUF3D in several ways. First, its integration into the CAD modeling environment in Rhino and the use of mesh-based surface discretization allows precise and detailed input geometry specification where surfaces may have arbitrary orientation and shape. ENVI-met and VTUF3D rely on a 3-D cartesian grid discretization that confines the geometry representation to a voxel space. While the voxels are not problematic per se, they limit the user's ability to counteract the N^2 complexity issue as the geometry will be forced to be simulated with identical resolution everywhere in the simulation domain. While we did not take advantage of the possibility of different sizes for mesh faces in this study, it would be easy to do so for larger models, thereby influencing the accuracy and simulation time even more favorably. Besides, the workflow presented has been implemented in Grasshopper, an algorithmic modeling environment for the widely used CAD software Rhinoceros that allows for modeling according to the principles of systems engineering.

This modular approach can easily be extended to consider long-wave radiation exchange with and between arbitrary patches with associated temperatures such as surfaces with vegetation, trees, and water features in the urban environment by simply adding an additional clustering layer that can group those surfaces by the similarity of their sensitive features. These surfaces could then be simulated by other models in EnergyPlus, such as the GreenRoofModel (Sailor, 2008), or with an entirely different tool that just provides corresponding annual surface temperatures that can be passed into to the Surfer algorithm. A workflow to produce leaf temperatures (Duursma & Medlyn, 2012) has been developed to streamline the modeling of the mean radiant temperatures from vegetative surfaces (Chokhachian & Hiller, 2020). Further studies are warranted to establish this link, as this is important for areas in which vegetation may not be neglected.

Further, the Surfer algorithm addresses a gap in software capabilities reported by Lee and Mayer (2016). They noted that their existing software considerably underestimated the T_{mrt} at low sun angles and suggested that not only multiple short-wave multiple reflections but also the long-wave radiant flux density emitted from the surrounding surfaces are crucial to estimate accurate $T_{mrt,}$ especially at low sun angles. The results in Table 4, particularly the discrepancies between results with and without long-wave radiation for the regions West (a) Bx2 and Bx3, confirm the claims made by Lee and Mayer (2016). We were able to show that the thermography measurements are in very good agreement with the simulation results of our method – even for highly localized phenomena. Hence, we believe the Surfer algorithm is capable of addressing the shortcoming identified by Lee and Mayer (2016), paired with a feasible amount of setup and computational effort.

In conclusion, it is worth noting that all previously developed surface temperature modeling schemas can benefit from the workflow introduced in this study. In Figure 2, we showed the limited inputs necessary for the framework to work, namely the building geometry and the associated materials, the number of clusters, and annual weather data in the EPW file format. As those inputs are common among other simulation engines, the Surfer workflow is poised to be integrated into existing workflows, such as estimating the impact of urban heat islands or mapping outdoor thermal comfort in urban areas. Although this work focuses on a case study of only a few buildings, our findings suggest that the simulation time for mean radiant temperature predictions at the urban scale can be significantly reduced while preserving model accuracy.

Conclusion

We introduce the Surfer algorithm, a fast simulation workflow to predict surface temperatures and mean radiant temperatures in large urban models. Estimating accurate mean radiant temperatures in urban areas requires an accurate estimation of the short- and long-wave radiative exchange between the sky and all participating building surfaces. When considering the long-wave radiation exchange, such efforts become computationally intractable for large urban areas due to their $O(N^2)$ complexity. Our algorithm discretizes all model surfaces and clusters them by material properties and sky and sun exposure to reduce computational complexity. We further take advantage of the K-Means clustering algorithm that is being trained on a novel set of features, including a virtual horizon for every participating mesh surface. We report a worst-case RMSE of 2°C for external surface temperatures for $k \geq 40$, comparing a high-fidelity simulation against the clustered approach while increasing the simulation time by a factor of 80, hence confirming our hypotheses stated above. Furthermore, a comparison against a real-world measurement at the authors' home institution shows that the clustered result is in good agreement with the real-world data, reporting an RMSE of 2.7 °C for seven days. The modular approach, the implementation into a visual programming environment called Grasshopper, and the tight integration with existing modeling frameworks such as EnergyPlus, and Radiance allows the Surfer algorithm to be seamlessly integrated into existing workflows that aim to estimate the mean radiant temperature in urban areas.

Acknowledgments

The authors would like to thank Cornell CTECH for supporting this work (US-DOT 69A3551747119).

Nomenclature

Variable	Description	Units
$\mathbf{q''_{LWR}}$	Exterior surface long-wave radiative heat flux	W/m^2
$\mathbf{q''_{conv}}$	Exterior surface convective heat flux	W/m^2
$\mathbf{q''_{cond}}$	Exterior surface conduction heat flux	W/m^2
$\mathbf{q''_{\alpha sol}}$	Exterior absorbed direct and diffuse solar (short-wave) radiation heat flux	W/m^2
hr	Linearized radiative heat transfer coefficient to air temperature	W/m^2*K
$\mathbf{t_{vis}}$	Visible transmittance	-
SHGC	Solar heat gain coefficient	-
$\mathbf{f_{eff}}$	Posture: standing, sitting, supine	-
$\mathbf{T_{surf}}$	Surface Outside face temperatures	K
$\mathbf{T_{air}}$	Outside air temperature	K
$\mathbf{T_{gnd}}$	Environmental ground surface temperature	K
$\mathbf{T_{sky}}$	Sky temperature	K
$\mathbf{F_{gnd}}$	view factor of wall surface to ground surface	-
$\mathbf{F_{sky}}$	View factor of wall surface to sky	-
$\mathbf{t_{sol}}$	Total solar transmittance	-
$\mathbf{f_{bes}}$	Fraction of body exposed to sun	-
K	Number of K-Means clusters	-
$\mathbf{F_{ij}}$	View factor from one mesh surface to another	-
$\mathbf{T_{mrt}}$	Mean radiant temperature	K
$\mathbf{S_1}$	First-order global sensitivity index	-
$\mathbf{S_2}$	Second-order global sensitivity index	-
$\mathbf{S_T}$	Total-order global sensitivity index	-
$\mathbf{F_{air}}$	View factor of wall surface to air	-
ε	Surface long-wave emissivity	-
σ	Stefan-Boltzmann constant	W/m2*K4

References

Allegrini, J., Kämpf, J., Dorer, V., & Carmeliet, J. (2013). *MODELLING THE URBAN MICROCLIMATE AND ITS INFLUENCE ON BUILDING ENERGY DEMANDS OF AN URBAN NEIGHBOURHOOD*. 6.

Arens, E., Hoyt, T., Zhou, X., Huang, L., Zhang, H., & Schiavon, S. (2015). Modeling the comfort effects of short-wave solar radiation indoors. *Building and Environment*, *88*, 3–9. https://doi.org/10.1016/j.buildenv.2014.09.004

Asawa, T., Hoyano, A., & Nakaohkubo, K. (2008). Thermal design tool for outdoor spaces based on heat balance simulation using a 3D-CAD system. *Building and Environment*, *43*(12), 2112–2123. https://doi.org/10.1016/j.buildenv.2007.12.007

Beckman, W. A., Broman, L., Fiksel, A., Klein, S. A., Lindberg, E., Schuler, M., & Thornton, J. (1994). TRNSYS The most complete solar energy system modeling and simulation software. *Renewable Energy*, *5*(1–4), 486–488.

Blazejczyk, K., Jendritzky, G., Broede, P., Fiala, D., Havenith, G., Epstein, Y., Psikuta, A., & Kampmann, B. (2013). *An introduction to the Universal Thermal Climate Index (UTCI)*. https://repository.lboro.ac.uk/articles/An_introduction_to_the_Universal_Thermal_Climate_Index_UTCI_/9347024

Bourgeois, D., Reinhart, C., & Ward, G. (2008). Standard daylight coefficient model for dynamic daylighting simulations. *Building Research & Information*, *36*(1), 68–82.

Chokhachian, A., & Hiller, M. (2020). *PANDO: Parametric Tool for Simulating Soil-Plant-Atmosphere of Tree Canopies in Grasshopper*. 8.

Coutts, A., Beringer, J., & Tapper, N. (2010). Changing Urban Climate and CO2 Emissions: Implications for the Development of Policies for Sustainable Cities. *Urban Policy and Research*, *28*(1), 27–47. https://doi.org/10.1080/08111140903437716

Crawley, D. B., Pedersen, C. O., Lawrie, L. K., & Winkelmann, F. C. (2000). EnergyPlus: Energy simulation program. *ASHRAE Journal*, *42*(4), 49.

Davies, M. G. (1994). The thermal response of an enclosure to periodic excitation: The CIBSE approach. *Building and Environment*, *29*(2), 217–235. https://doi.org/10.1016/0360-1323(94)90072-8

De Dear, R. (1988). Ping-pong globe thermometers for mean radiant temperatures. *H and V Engineer*, *60*(681), 10–11.

DoE, U. (2010). Energyplus engineering reference. *The Reference to Energyplus Calculations*.

Dogan, T., & Reinhart, C. (2017). Shoeboxer: An algorithm for abstracted rapid multi-zone urban building energy model generation and simulation. *Energy and Buildings*, *140*, 140–153. https://doi.org/10.1016/j.enbuild.2017.01.030

Duursma, R. A., & Medlyn, B. E. (2012). MAESPA: A model to study interactions between water limitation, environmental drivers and vegetation function at tree and stand levels, with an example application to [CO_2] × drought interactions. *Geoscientific Model Development*, *5*(4), 919–940. https://doi.org/10.5194/gmd-5-919-2012

Engineering ToolBox. (2009). *Absorbed Solar Radiation*. https://www.engineeringtoolbox.com/solar-radiation-absorbed-materials-d_1568.html

Evins, R., Dorer, V., & Carmeliet, J. (2014). Simulating external longwave radiation exchange for buildings. *Energy and Buildings*, *75*, 472–482.

Gagliano, A., Detommaso, M., & Nocera, F. (2017). Assessment of the Green Roofs Thermal Dynamic Behavior for Increasing the Building Energy Efficiencies. In J. Littlewood, C. Spataru, R. J. Howlett, & L. C. Jain (Eds.), *Smart Energy Control Systems for Sustainable Buildings* (Vol. 67, pp. 37–59). Springer International Publishing. https://doi.org/10.1007/978-3-319-52076-6_2

Gál, C. V., & Nice, K. A. (2020). *MEAN RADIANT TEMPERATURE MODELING OUTDOORS: A COMPARISON OF THREE APPROACHES*. 10.

Ghandehari, M., Emig, T., & Aghamohamadnia, M. (2018). Surface temperatures in New York City: Geospatial data enables the accurate prediction of radiative heat transfer. *Scientific Reports*, *8*(1), 1–10.

Grilo, F., Pinho, P., Aleixo, C., Catita, C., Silva, P., Lopes, N., Freitas, C., Santos-Reis, M., McPhearson, T., & Branquinho, C. (2020). Using green to cool the grey: Modelling the cooling effect of green spaces with a high spatial resolution. *Science of The Total Environment*, *724*, 138182. https://doi.org/10.1016/j.scitotenv.2020.138182

Grimmond, C. S. B., Blackett, M., Best, M. J., Barlow, J., Baik, J.-J., Belcher, S. E., Bohnenstengel, S. I., Calmet, I., Chen, F., Dandou, A., Fortuniak, K., Gouvea, M. L., Hamdi, R., Hendry, M., Kawai, T., Kawamoto, Y., Kondo, H., Krayenhoff, E. S., Lee, S.-H., … Zhang, N. (2010). The International Urban Energy Balance Models Comparison Project: First Results from Phase 1. *Journal of Applied Meteorology and Climatology*, *49*(6), 1268–1292. https://doi.org/10.1175/2010JAMC2354.1

Hardy, A., & Steeb, W.-H. (2008). *Mathematical tools in computer graphics with C# implementations*. World Scientific Publishing Company.

Herman, J., & Usher, W. (2017). SALib: An open-source python library for sensitivity analysis. *The Journal of Open Source Software*, *2*(9). https://doi.org/10.21105/joss.00097

Konopacki, S., Gartland, L., Akbari, H., & Rainer, L. (1998). *Demonstration of energy savings of cool roofs*. https://doi.org/10.2172/296885

Kottek, M., Grieser, J., Beck, C., Rudolf, B., & Rubel, F. (2006). World map of the Köppen-Geiger climate classification updated. *Meteorologische Zeitschrift*, *15*(3), 259–263.

Krayenhoff, E. S., Moustaoui, M., Broadbent, A. M., Gupta, V., & Georgescu, M. (2018). Diurnal interaction between urban expansion, climate change and adaptation in US cities. *Nature Climate Change*, *8*(12), 1097–1103. https://doi.org/10.1038/s41558-018-0320-9

Krayenhoff, E. S., & Voogt, J. A. (2007). A microscale three-dimensional urban energy balance model for studying surface temperatures. *Boundary-Layer Meteorology*, *123*(3), 433–461. https://doi.org/10.1007/s10546-006-9153-6

Lee, H., & Mayer, H. (2016). Validation of the mean radiant temperature simulated by the RayMan software in urban environments. *International Journal of Biometeorology*, *60*(11), 1775–1785. https://doi.org/10.1007/s00484-016-1166-3

Lindberg, F., Holmer, B., & Thorsson, S. (2008). SOLWEIG 1.0–Modelling spatial variations of 3D radiant fluxes and mean radiant temperature in complex urban settings. *International Journal of Biometeorology*, *52*(7), 697–713.

Liu, J., Heidarinejad, M., Nikkho, S. K., Mattise, N. W., & Srebric, J. (2019). Quantifying Impacts of Urban Microclimate on a Building Energy Consumption—A Case Study. *Sustainability*, *11*(18), 4921. https://doi.org/10.3390/su11184921

Luo, X., Hong, T., & Tang, Y.-H. (2020). Modeling Thermal Interactions between Buildings in an Urban Context. *Energies*, *13*(9), 2382. https://doi.org/10.3390/en13092382

Mackey, C., Galanos, T., Norford, L., Roudsari, M. S., & Architects, P. (2017). *Wind, Sun, Surface Temperature, and Heat Island: Critical Variables for High-Resolution Outdoor Thermal Comfort*. 9.

MacQueen, J. (1967). Some methods for classification and analysis of multivariate observations. *Proceedings of the Fifth Berkeley Symposium on Mathematical Statistics and Probability, Volume 1: Statistics*, 281–297. https://projecteuclid.org/euclid.bsmsp/1200512992

Matzarakis, A., Rutz, F., & Mayer, H. (2007). Modelling radiation fluxes in simple and complex environments—Application of the RayMan model. *International Journal of Biometeorology*, *51*(4), 323–334.

Mayer, H., & Höppe, P. (1987). Thermal comfort of man in different urban environments. *Theoretical and Applied Climatology*, *38*(1), 43–49.

Metzger, K. B., Ito, K., & Matte, T. D. (2010). Summer heat and mortality in New York City: How hot is too hot? *Environmental Health Perspectives*, *118*(1), 80–86.

Miller, C., Thomas, D., Kämpf, J., & Schlueter, A. (2015). Long wave radiation exchange for urban scale modelling within a co-simulation environment. *Proceedings of International Conference CISBAT 2015 Future Buildings and Districts Sustainability from Nano to Urban Scale*, *CONF*, 871–876.

Nice, K. A., Coutts, A. M., & Tapper, N. J. (2018). Development of the VTUF-3D v1.0 urban micro-climate model to support assessment of urban vegetation influences on human thermal comfort. *Urban Climate*, *24*, 1052–1076. https://doi.org/10.1016/j.uclim.2017.12.008

Nikolopoulou et al. - 1999—Improvements to the Globe Thermometer for Outdoor .pdf. (n.d.).

Perini, K., Chokhachian, A., Dong, S., & Auer, T. (2017). Modeling and simulating urban outdoor comfort: Coupling ENVI-Met and TRNSYS by grasshopper. *Energy and Buildings*, *152*, 373–384. https://doi.org/10.1016/j.enbuild.2017.07.061

Reindl, D. T., Beckman, W. A., & Duffie, J. A. (1990). Diffuse fraction correlations. *Solar Energy*, *45*(1), 1–7. https://doi.org/10.1016/0038-092X(90)90060-P

Sailor, D. J. (2008). A green roof model for building energy simulation programs. *Energy and Buildings*, *40*(8), 1466–1478.

Saltelli, A., Annoni, P., Azzini, I., Campolongo, F., Ratto, M., & Tarantola, S. (2010). Variance based sensitivity analysis of model output. Design and estimator for the total sensitivity

index. *Computer Physics Communications*, *181*(2), 259–270. https://doi.org/10.1016/j.cpc.2009.09.018

Santamouris, M., Gaitani, N., Spanou, A., Saliari, M., Giannopoulou, K., Vasilakopoulou, K., & Kardomateas, T. (2012). Using cool paving materials to improve microclimate of urban areas – Design realization and results of the flisvos project. *Building and Environment*, *53*, 128–136. https://doi.org/10.1016/j.buildenv.2012.01.022

Sobol, I. M. (2001). Global sensitivity indices for nonlinear mathematical models and their Monte Carlo estimates. *Mathematics and Computers in Simulation*, *55*(1), 271–280. https://doi.org/10.1016/S0378-4754(00)00270-6

Solemma LLC. (2019). *ClimateStudio* (Version 1) [Computer software]. Solemma LLC. http://solemma.com

Subramaniam, S. (2017). Daylighting Simulations with Radiance using Matrix-based Methods. *Lawrence Berke-Ley National Laboratory*.

Talbot, C., Bou-Zeid, E., & Smith, J. (2012). Nested mesoscale large-eddy simulations with WRF: Performance in real test cases. *Journal of Hydrometeorology*, *13*(5), 1421–1441.

Taleghani, M. (2018). The impact of increasing urban surface albedo on outdoor summer thermal comfort within a university campus. *Urban Climate*, *24*, 175–184. https://doi.org/10.1016/j.uclim.2018.03.001

Thorndike, R. L. (1953). Who belongs in the family? *Psychometrika*, *18*(4), 267–276. https://doi.org/10.1007/BF02289263

Thorsson, S., Lindberg, F., Eliasson, I., & Holmer, B. (2007). Different methods for estimating the mean radiant temperature in an outdoor urban setting. *International Journal of Climatology: A Journal of the Royal Meteorological Society*, *27*(14), 1983–1993.

Yang, X., & Li, Y. (2013). Development of a Three-Dimensional Urban Energy Model for Predicting and Understanding Surface Temperature Distribution. *Boundary-Layer Meteorology*, *149*(2), 303–321. https://doi.org/10.1007/s10546-013-9842-x